



NRL/MR/6790--13-9459

# **Fully Explicit Nonlinear Optics Model in a Particle-in-Cell Framework**

D.F. GORDON

M.H. HELLE

J.R. PEÑANO

*Beam Physics Branch  
Plasma Physics Division*

April 19, 2013

Approved for public release; distribution is unlimited.

<b>REPORT DOCUMENTATION PAGE</b>				<b>Form Approved OMB No. 0704-0188</b>	
Public reporting burden for this collection of information is estimated to average 1 hour per response, including the time for reviewing instructions, searching existing data sources, gathering and maintaining the data needed, and completing and reviewing this collection of information. Send comments regarding this burden estimate or any other aspect of this collection of information, including suggestions for reducing this burden to Department of Defense, Washington Headquarters Services, Directorate for Information Operations and Reports (0704-0188), 1215 Jefferson Davis Highway, Suite 1204, Arlington, VA 22202-4302. Respondents should be aware that notwithstanding any other provision of law, no person shall be subject to any penalty for failing to comply with a collection of information if it does not display a currently valid OMB control number. <i>PLEASE DO NOT RETURN YOUR FORM TO THE ABOVE ADDRESS.</i>					
<b>1. REPORT DATE (DD-MM-YYYY)</b> 19-04-2013		<b>2. REPORT TYPE</b> Interim		<b>3. DATES COVERED (From - To)</b> October 2009 – October 2012	
<b>4. TITLE AND SUBTITLE</b>  Fully Explicit Nonlinear Optics Model in a Particle-in-Cell Framework				<b>5a. CONTRACT NUMBER</b>	
				<b>5b. GRANT NUMBER</b>	
				<b>5c. PROGRAM ELEMENT NUMBER</b>	
<b>6. AUTHOR(S)</b>  D.F. Gordon, M.H. Helle, and J.R. Peñano				<b>5d. PROJECT NUMBER</b> 67-9869-03	
				<b>5e. TASK NUMBER</b>	
				<b>5f. WORK UNIT NUMBER</b>	
<b>7. PERFORMING ORGANIZATION NAME(S) AND ADDRESS(ES)</b>  Naval Research Laboratory 4555 Overlook Avenue, SW Washington, DC 20375-5320				<b>8. PERFORMING ORGANIZATION REPORT NUMBER</b>  NRL/MR/6790--13-9459	
<b>9. SPONSORING / MONITORING AGENCY NAME(S) AND ADDRESS(ES)</b>  Office of Naval Research 875 North Randolph Street, Suite 1425 Arlington, VA 22203-1995				<b>10. SPONSOR / MONITOR'S ACRONYM(S)</b>  ONR	
				<b>11. SPONSOR / MONITOR'S REPORT NUMBER(S)</b>	
<b>12. DISTRIBUTION / AVAILABILITY STATEMENT</b>  Approved for public release; distribution is unlimited.					
<b>13. SUPPLEMENTARY NOTES</b>					
<b>14. ABSTRACT</b>  A numerical technique which incorporates the nonlinear optics of anisotropic crystals into a particle-in-cell framework is described. The model is useful for simulating interactions between crystals, ultra-short laser pulses, intense relativistic electron bunches, plasmas, or any combination thereof. The frequency content of the incident and scattered radiation is limited only by the resolution of the spatial and temporal grid. A numerical stability analysis indicates that the Courant condition is more stringent than in the vacuum case. Numerical experiments are carried out illustrating the electro-optic effect, soliton propagation, and the generation of fields in a crystal by a relativistic electron bunch.					
<b>15. SUBJECT TERMS</b> Nonlinear optics                      Particle-in-cell Electro-optic sensing					
<b>16. SECURITY CLASSIFICATION OF:</b>			<b>17. LIMITATION OF ABSTRACT</b>  Unclassified Unlimited	<b>18. NUMBER OF PAGES</b>  27	<b>19a. NAME OF RESPONSIBLE PERSON</b> Daniel F. Gordon
<b>a. REPORT</b> Unclassified Unlimited	<b>b. ABSTRACT</b> Unclassified Unlimited	<b>c. THIS PAGE</b> Unclassified Unlimited			<b>19b. TELEPHONE NUMBER (include area code)</b> (202) 767-5036

# Fully Explicit Nonlinear Optics Model in a Particle-in-Cell Framework

D.F. Gordon, M.H. Helle, and J.R. Peñano

*Beam Physics Branch, Plasma Physics Division*

A numerical technique which incorporates the nonlinear optics of anisotropic crystals into a particle-in-cell framework is described. The model is useful for simulating interactions between crystals, ultra-short laser pulses, intense relativistic electron bunches, plasmas, or any combination thereof. The frequency content of the incident and scattered radiation is limited only by the resolution of the spatial and temporal grid. A numerical stability analysis indicates that the Courant condition is more stringent than in the vacuum case. Numerical experiments are carried out illustrating the electro-optic effect, soliton propagation, and the generation of fields in a crystal by a relativistic electron bunch.

## Contents

<b>I. Introduction</b>	1
<b>II. Description of the Model</b>	2
<b>III. Analytical Dispersion Relation</b>	3
<b>IV. Oscillator Parameters</b>	4
<b>V. Numerical Technique</b>	7
A. Oscillator Equation and Source Deposition	7
B. Linear Stability and Accuracy	9
C. Nonlinear Stability	10
D. False Resonance Technique for Accelerating Computation	12
E. Boundary Conditions and Moving Window	13
<b>VI. Numerical Experiments</b>	14
A. Electro-Optic Effect	14
B. Soliton Propagation	15
C. Electron Bunch Passing Near a Crystal	19
<b>VII. Conclusions</b>	22
<b>VIII. Acknowledgements</b>	22
<b>References</b>	23
<b>Appendix</b>	25

## I. INTRODUCTION

Nonlinear optics is often described in the frequency domain so that dispersive effects can be treated in a simple way. The convolution integrals associated with nonlinear effects are simplified by assuming that the radiation spectrum takes the form of a discrete set of narrow peaks. In the case of few cycle pulses, the convolution integrals cannot be reduced, and a time domain model becomes attractive. The finite-difference-time-domain (FDTD) technique is a well established method for solving the exact Maxwell equations in a bounded or periodic domain [1]. It may be used in connection with the particle-in-cell (PIC) technique to self-consistently solve for the motions of a large number of charged particles in an electromagnetic field [2]. This approach is often used to model fully nonlinear laser-plasma interactions and beam-plasma interactions. In this work, it is extended to account for nonlinear laser-crystal and beam-crystal interactions. This is accomplished by incorporating a model for bound particles into the PIC code turboWAVE [3]. The model is fully parallelized, and runs in up to three dimensions.

The PIC aspect of turboWAVE has much in common with a number of other codes designed to model laser-plasma interactions [4–10]. The nonlinear optics aspect is related to a number of other codes designed to model ultrashort pulse propagation in a nonlinear medium [11–16]. Both types of codes can be divided into those that describe the radiation by means of a complex envelope, and those that are fully explicit, i.e., those that resolve the optical time scale. TurboWAVE supports both models, but in this work only the fully explicit model is used. As a result, there is no assumption about the frequency content of the radiation, and given the right model for the dielectric response, all nonlinear and dispersive effects are accounted for.

Our model for the dielectric response generalizes the auxiliary equation technique described in Refs. [13, 15]. In particular, bound charges in the dielectric are represented by effective particles, whose contribution to the four-current is computed using PIC techniques. The effective particles are subjected to forces arising from a superposition of macroscopic and microscopic fields. The macroscopic field is the usual electromagnetic field that is computed in any FDTD code, while the microscopic field is a three dimensional electrostatic potential representing, e.g., an atomic binding potential. The resulting equation of motion is expanded as an anharmonic oscillator equation. By using multiple species of effective particles, each

satisfying a different oscillator equation, the material response can be tailored to match that of real materials over a broad range of frequencies. Free charges are self-consistently incorporated into the model by linear superposition of the free and bound sources in the FDTD field solver [36]. The resulting model is capable of modeling interactions among laser pulses, particle beams, plasmas, and dielectric crystals, in a fully dispersive, nonlinear, anisotropic, and kinetic way.

In Ref. [17], the turboWAVE extensions described in this report were introduced for the first time. In Ref. [18], the model was applied to a novel electro-optic diagnostic technique. In the present report, the model is described in more detail, and a formal analysis of numerical stability is given. The model is extended to include third order nonlinearities, and the implementation is demonstrated via three numerical experiments.

## II. DESCRIPTION OF THE MODEL

The numerical model described here solves the exact Maxwell equations:

$$\nabla \times \mathbf{H} = \mathbf{J} + \frac{\partial \mathbf{D}}{\partial t} \quad (1a)$$

$$\nabla \times \mathbf{E} = -\frac{\partial \mathbf{B}}{\partial t} \quad (1b)$$

$$\nabla \cdot \mathbf{D} = \rho \quad (1c)$$

$$\nabla \cdot \mathbf{B} = 0 \quad (1d)$$

Here,  $\mathbf{B} = \mu_0 \mathbf{H} + \mathbf{M}$  and  $\mathbf{D} = \epsilon_0 \mathbf{E} + \mathbf{P}$ , where  $\mathbf{P}$  is the polarization and  $\mathbf{M}$  is the magnetization. In the present work, we take  $\mathbf{M} = 0$ . The polarization can be expressed in terms of a spatially smoothed four-current due to bound charges, denoted by  $(\langle \eta \rangle, \langle \mathbf{j} \rangle)$ . This results in [19]

$$\nabla \times \mathbf{B} = \mu_0 (\mathbf{J} + \langle \mathbf{j} \rangle) + \frac{1}{c^2} \frac{\partial \mathbf{E}}{\partial t} \quad (2a)$$

$$\nabla \times \mathbf{E} = -\frac{\partial \mathbf{B}}{\partial t} \quad (2b)$$

$$\nabla \cdot \mathbf{E} = (\rho + \langle \eta \rangle) / \epsilon_0 \quad (2c)$$

$$\nabla \cdot \mathbf{B} = 0 \quad (2d)$$

With this formulation, any field solver designed to account for free charges can be easily adapted to account for bound charges by making the substitution

$$(\rho, \mathbf{J}) \rightarrow (\rho + \langle \eta \rangle, \mathbf{J} + \langle \mathbf{j} \rangle) \quad (3)$$

Our model for  $(\langle \eta \rangle, \langle \mathbf{j} \rangle)$  is based on calculating the motions of effective particles that respond to the superposition of a microscopic binding potential and a macroscopic electric field  $\mathbf{E}$ . Denoting the displacement of an effective particle from its equilibrium position by  $\mathbf{r}$ , and expanding the microscopic potential in a Taylor series, results in the effective particle equation of motion

$$\frac{\partial^2 r_i}{\partial t^2} + \sum_{jk} \left[ 2\Gamma_{ij} \frac{\partial r_j}{\partial t} + (\Omega^2)_{ij} r_j + a_{ijk} r_j r_k - b r_i r_j r_j \right] = \frac{q}{m} E_i \quad (4)$$

where the subscripts vary over Cartesian coordinates, and  $q/m$  is the charge to mass ratio. The anisotropy of the medium is represented by the tensors  $\Gamma$ ,  $\Omega^2$ , and  $\mathbf{a}$ . These are, respectively, the damping rate, the square of the resonant frequency, and the first anharmonic coefficient. At present, the second anharmonic coefficient,  $b$ , is assumed scalar. By means of a coordinate transformation,  $\Omega^2$  can always be made diagonal. The basis vectors which induce this transformation will be denoted by  $(\mathbf{e}_u, \mathbf{e}_v, \mathbf{e}_w)$ . The basis vectors used for the general calculation will be denoted  $(\mathbf{e}_x, \mathbf{e}_y, \mathbf{e}_z)$ . The crystallographic basis vectors, which generally coincide with  $(\mathbf{e}_u, \mathbf{e}_v, \mathbf{e}_w)$ , are denoted  $(\langle 100 \rangle, \langle 010 \rangle, \langle 001 \rangle)$ .

In general, the parameters in Eq. (4) depend not only on tensor indices, but also on an index  $p$  that identifies a particular particle. In other words, each particle may move in a unique potential well, and may therefore satisfy a unique equation of motion. The system of the particle together with its equation of motion is called an oscillator. In practical implementations, it is convenient to group all particles that satisfy the same equation of motion into an oscillator species with index  $s$ . Then the material parameters,  $q$ ,  $m$ ,  $\Omega^2$ ,  $\Gamma$ ,  $\mathbf{a}$ , and  $b$ , depend on  $s$ , while only  $\mathbf{r}$  is explicitly dependent on  $p$ . As discussed below, the macroscopic sources  $(\langle \eta \rangle, \langle \mathbf{j} \rangle)$  can be derived from the set  $\mathbf{r}_p$  using a variation on source deposition techniques developed for PIC codes.

### III. ANALYTICAL DISPERSION RELATION

In order to analyze the model described above, consider the locally averaged displacement  $\langle \mathbf{r}_s \rangle$  associated with each oscillator species. In the case of a uniform medium, this is related

to the spatially smoothed four-current by

$$(\langle \eta \rangle, \langle \mathbf{j} \rangle) = \sum_s q_s N_s \left( -\nabla \cdot \mathbf{f} \langle \mathbf{r}_s \rangle, \frac{\partial}{\partial t} \mathbf{f} \langle \mathbf{r}_s \rangle \right) \quad (5)$$

where  $N_s$  is the density of oscillators, and the tensor  $\mathbf{f}$  is an oscillator strength. Assuming local phase coherence,  $\langle \mathbf{r}_s \rangle$  satisfies the same equation as  $\mathbf{r}_p$ , which in the  $(\mathbf{e}_u, \mathbf{e}_v, \mathbf{e}_w)$  basis is

$$\left( \frac{\partial^2}{\partial t^2} + 2\Gamma_{iis} \frac{\partial}{\partial t} + \Omega_{iis}^2 \right) \langle r_{is} \rangle = -\frac{q_s}{m_s} \left( \frac{\partial A_i}{\partial t} + \frac{\partial \phi}{\partial \xi_i} \right). \quad (6)$$

where  $i$  is the coordinate index,  $\xi_i$  is the  $i^{\text{th}}$  coordinate,  $\mathbf{A}$  is the vector potential, and  $\phi$  is the scalar potential. Using the Coulomb gauge, the radiation is described by

$$\left( c^2 \nabla^2 - \frac{\partial^2}{\partial t^2} \right) A_i = -\sum_s f_{iis} \frac{q_s N_s}{\epsilon_0} \frac{\partial \langle r_{is} \rangle}{\partial t} + \frac{\partial^2 \phi}{\partial t \partial \xi_i} \quad (7)$$

Consider any mode with a wave-vector that is collinear with one of the principal axes,  $(\mathbf{e}_u, \mathbf{e}_v, \mathbf{e}_w)$ . Then, it can be shown that  $\phi = 0$ , and the transverse components of  $\mathbf{A}$  satisfy the dispersion relation

$$\omega^2 \left( 1 + \sum_s \frac{f_{iis} \omega_{ps}^2}{\mathcal{D}_{is}(\omega)} \right) - c^2 k^2 = 0 \quad (8)$$

where  $\omega_{ps}^2 = N_s q_s^2 / \epsilon_0 m_s$ , and

$$\mathcal{D}_{is}(\omega) = \Omega_{iis}^2 - 2i\omega\Gamma_{iis} - \omega^2 \quad (9)$$

In the case of a medium comprised of a single, lossless, isotropic species with unit oscillator strength, the dispersion relation is

$$(\Omega^2 - \omega^2)(\omega^2 - c^2 k^2) + \omega^2 \omega_p^2 = 0 \quad (10)$$

The primary feature of this dispersion relation is a stop-band between the resonant frequency,  $\Omega$ , and the cutoff frequency,  $\sqrt{\Omega^2 + \omega_p^2}$ .

#### IV. OSCILLATOR PARAMETERS

Measured dielectric properties are usually given as susceptibilities in the frequency domain. Hence, in order to apply the time dependent model described above to real materials, it is necessary to connect the constants  $\Omega^2$ ,  $\Gamma$ ,  $\mathbf{f}$ ,  $\mathbf{a}$ , and  $b$ , with the susceptibilities



Parameter	Lattice Oscillator	Electronic Oscillator
Oscillator Strength, $f$	1	1
Resonance Frequency, $\Omega$	$6.90 \times 10^{13}$ rad/s	$6.38 \times 10^{15}$ rad/s
Damping Frequency, $\Gamma$	$6.25 \times 10^{10}$ rad/s	0
Plasma Frequency, $\omega_p$	$9.27 \times 10^{13}$ rad/s	$1.78 \times 10^{16}$ rad/s
Anharmonic Coefficient, $a_{123}$	$-3.28 \times 10^{37}$ m <sup>-1</sup> s <sup>-2</sup>	$4.1 \times 10^{41}$ m <sup>-1</sup> s <sup>-2</sup>

TABLE I: Oscillator Parameters for Gallium Phosphide

$\chi^{(n)}(\omega_1, \omega_2, \dots)$ . In the  $(\mathbf{e}_u, \mathbf{e}_v, \mathbf{e}_w)$  basis, the linear susceptibility has only the diagonal elements

$$\chi_{ii}(\omega) = \sum_s \frac{f_{is}\omega_{ps}^2}{\mathcal{D}_{is}(\omega)} \quad (11)$$

Following Ref. [20], the first anharmonic coefficient is related to  $\chi^{(2)}$  by

$$\chi_{ijk}^{(2)}(\omega_1, \omega_2, \omega_3) = - \sum_s \frac{q_s}{m_s} \frac{f_s \omega_{ps}^2}{\mathcal{D}_s(\omega_1) \mathcal{D}_s(\omega_2) \mathcal{D}_s(\omega_3)} (a_{ijk})_s \quad (12)$$

where for simplicity, a cubic crystal is assumed. The nonlinear susceptibility is related to the electro-optic coefficient  $r_{ijk}$  via

$$\chi_{ijk}^{(2)}(\omega + \delta\omega, \omega, \delta\omega) = -\frac{1}{2} \sum_{lm} \epsilon_{il}(\omega) r_{lmk}(\omega, \delta\omega) \epsilon_{mj}(\omega) \quad (13)$$

Here, the factor of 1/2 accounts for the degeneracy of sum and difference generation when  $\delta\omega \rightarrow 0$ , and  $\epsilon$  is the relative permittivity. Finally, the nonlinear refractive index is given by

$$n_2(\omega) = \frac{3}{4} \frac{\eta_0}{n_0(\omega)^2} \sum_s \frac{q_s^2}{m_s^2} \frac{\omega_{ps}^2}{\mathcal{D}_s^*(\omega) \mathcal{D}_s(\omega)^3} b_s \quad (14)$$

where  $n_0$  is the linear refractive index and  $\eta_0$  is the impedance of free space (see appendix). Note that the charge to mass ratio  $q_s/m_s$  amounts to an extraneous free parameter that could have been absorbed into  $q_s N_s$ ,  $\mathbf{a}_s$ , and  $b_s$ . In this work, the electronic charge to mass ratio is always assumed.

As an example, consider the cubic crystal gallium phosphide (GaP), which is useful for electro-optic sensing applications [24–28]. Expressions fitting the measured linear dispersion have already been given in Ref. [21]. There, two separate expressions were used for the optical and THz regimes. A two-oscillator model based on the parameters given in Table I, agrees with both expressions, as illustrated in Figs. 1(a) and (b).

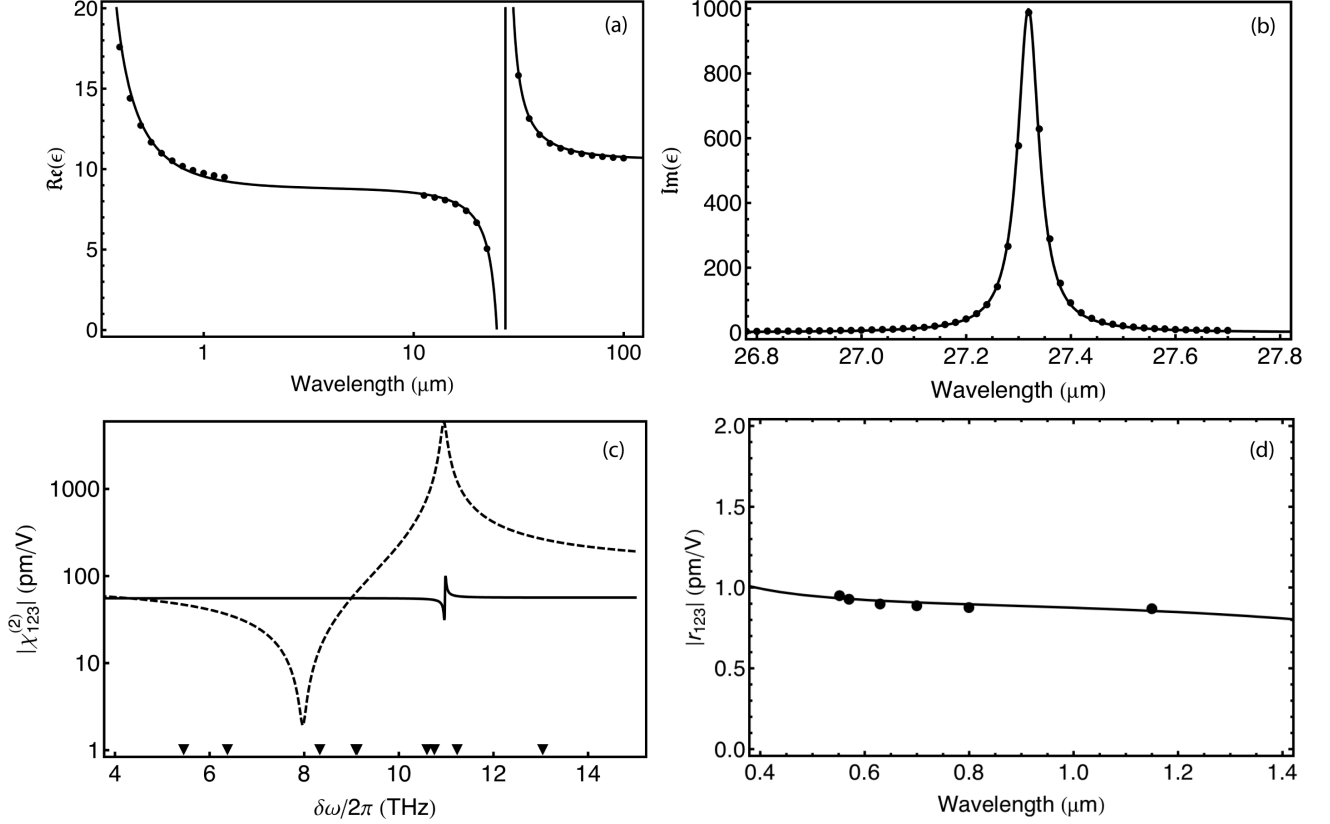


FIG. 1: Nonlinear Lorentz model for GaP. Panel (a) displays  $\Re(\epsilon)$ , where the solid curve is the two-oscillator (2O) model and the points are from the expressions in Ref. [21]. Panel (b) is similar to (a) except  $\Im(\epsilon)$  is displayed. Panel (c) displays  $\chi_{123}^{(2)}(\omega_L \pm \delta\omega, \omega_L, \delta\omega)$ , where  $\omega_L$  is a probe laser frequency, given by  $2\pi c/\omega_L = 0.6328 \mu\text{m}$ . The solid curve is the 2O model, and the dashed curve is the expression in Ref. [22]. The triangles indicate the infra-red frequencies where the data points in [22] are located. Panel (d) displays  $r_{123}(\omega, \delta\omega) = r_{41}(\omega, \delta\omega)$ , where  $\delta\omega \rightarrow 0$ . The curve is the 2O model, and the points are the data from Ref. [23]. The 2O model cannot be made consistent with both Refs. [22] and [23].

Once the linear dispersion is determined, the only remaining free parameters are the anharmonic coefficients associated with each oscillator. In order to choose these parameters, an attempt was made to simultaneously fit data from Refs. [22] and [23]. In Ref. [22],  $\chi_{ijk}^{(2)}(\omega_L \pm \delta\omega, \omega_L, \delta\omega)$  is reported, where  $\omega_L$  is the frequency of a probing helium-neon laser, and  $\delta\omega$  is one of several infra-red frequencies produced by a multi-line  $\text{H}_2+\text{O}_2$  laser. In Ref. [23],  $r_{ijk}(\omega, \delta\omega)$  is measured, where  $\delta\omega$  is in the radio frequency (RF) range, and  $\omega$  takes several values in the optical range. It was found that the two-oscillator model cannot

be made to agree with both experiments. The parameters of Table I are chosen to obtain agreement with the measured  $r_{ijk}(\omega, \delta\omega)$ . The resulting dispersion is displayed in Figs. 1(c) and (d). In order to make the two-oscillator model agree with  $\chi^{(2)}(\omega_L \pm \delta\omega, \omega_L, \delta\omega)$ , a much larger absolute value of the lattice anharmonic coefficient must be used. This leads, roughly, to the oscillator parameters given in Ref. [17], although for the simulations presented there and in Ref. [18], the lattice oscillator was taken to be linear.

## V. NUMERICAL TECHNIQUE

### A. Oscillator Equation and Source Deposition

Most electromagnetic PIC codes use the leap-frog technique. More specifically,  $\mathbf{E}^{n+1}$  is computed using  $\mathbf{E}^n$ ,  $\mathbf{B}^{n+\frac{1}{2}}$  and  $\mathbf{J}^{n+\frac{1}{2}}$ , where  $n$  is the time level. Then,  $\mathbf{B}^{n+\frac{3}{2}}$  is computed using  $\mathbf{B}^{n+\frac{1}{2}}$  and  $\mathbf{E}^{n+1}$ . In some cases a Poisson solver is used to refine  $\mathbf{E}^{n+1}$  using  $\rho^{n+1}$ . As discussed above, any such field solver can be used in the presence of an oscillator population by making the substitution  $(\rho, \mathbf{J}) \rightarrow (\rho + \langle \eta \rangle, \mathbf{J} + \langle \mathbf{j} \rangle)$ . This implies that  $\langle \eta \rangle$  is known at integral time levels, and  $\langle \mathbf{j} \rangle$  is known at half-integral time levels.

To compute  $\langle \eta \rangle^{n+1}$  and  $\langle \mathbf{j} \rangle^{n+\frac{1}{2}}$ , the displacements  $\mathbf{r}_p^n$  and  $\mathbf{r}_p^{n+1}$  are needed. Let  $\mathbf{T}$  represent the matrix of transformation of a vector from the  $(\mathbf{e}_u, \mathbf{e}_v, \mathbf{e}_w)$  basis to the  $(\mathbf{e}_x, \mathbf{e}_y, \mathbf{e}_z)$  basis. If all quantities characterizing the oscillators are stored in the  $(\mathbf{e}_u, \mathbf{e}_v, \mathbf{e}_w)$  basis, the displacements can be updated using

$$\frac{r_i^{n+1} - 2r_i^n + r_i^{n-1}}{\Delta t^2} + 2\Gamma_{ii}\frac{r_i^{n+1} - r_i^n}{\Delta t} + (\Omega^2)_{ii}r_i^n = \frac{F_i^n}{m} \quad (15)$$

where  $\Delta t$  is the time step and

$$\mathbf{F}^n = q\mathbf{T}^{-1}\mathbf{E}^n - m\mathbf{a}\mathbf{r}^n\mathbf{r}^n + mb(\mathbf{r}^n \cdot \mathbf{r}^n)\mathbf{r}^n \quad (16)$$

The macroscopic four-current  $(\langle \eta \rangle, \langle \mathbf{j} \rangle)$  associated with the microscopic orbits  $\mathbf{r}_p^n$  can be computed using PIC techniques. These techniques regard each particle as a “cloud” with dimensions on the order of a cell size. Knowing the orbit of each cloud’s centroid allows one to compute the amount of charge in each cell as a function of time, as well as the current passing through each cell wall. Various schemes have been developed to facilitate this calculation [2, 29, 30]. In the case of bound charges, these schemes have to be applied with care in order to minimize round-off errors associated with very small displacements.

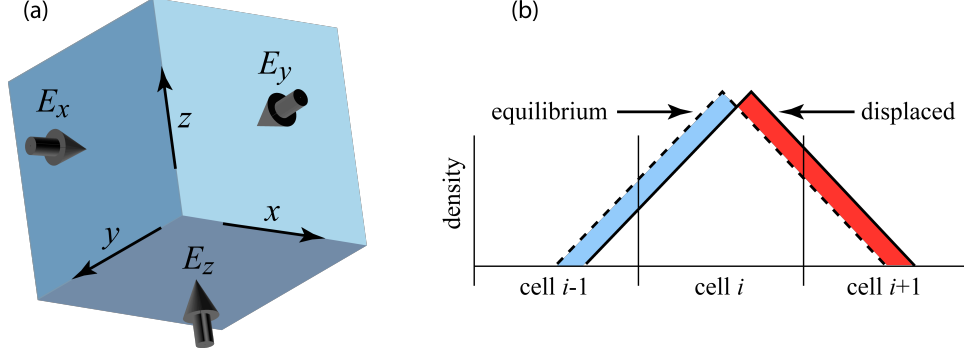


FIG. 2: Charge Deposition. (a) Geometry of a grid cell in relation to the points on the Yee mesh. The three dimensional arrows point to the mesh points where the corresponding electric field components are known. (b) Quadratic Weighting. The bound charges are represented by charge clouds (solid curve) whose equilibrium position (dashed curve) is the centroid of the cell volume. For an electron, the charge in a cell is increased (decreased) by the area of the intersection of the blue (red) area with the cell.

To deposit the sources due to bound charges, place one oscillator, per species, in each grid cell [37]. The cell geometry is shown in Fig. 2(a). The deposition of charge, in one dimension, is illustrated in Fig. 2(b). The oscillator is represented by two oppositely charged density distributions. The equilibrium distribution, shown as a dashed line, is immobile. The displaced distribution, shown as a solid line, executes the orbit described by Eq. (15). The net charge in a cell is the integral over the cell volume of the difference between the distributions. To minimize round-off error, this integral should *not* be carried out by re-using a PIC routine that deposits each distribution separately. Instead, expressions should be written for the net charge in a cell, and expanded to lowest order in the displacement. Then, for the oscillator in cell  $(i, j, k)$ , the net charge density is distributed in the surrounding cells as follows:

$$\langle \eta \rangle_{i\pm 1, j, k}^n = \pm \mathbf{e}_x \cdot \mathbf{Tf} \mathbf{r}_p^n \frac{N_s q_s}{2\Delta x} \quad (17a)$$

$$\langle \eta \rangle_{i, j\pm 1, k}^n = \pm \mathbf{e}_y \cdot \mathbf{Tf} \mathbf{r}_p^n \frac{N_s q_s}{2\Delta y} \quad (17b)$$

$$\langle \eta \rangle_{i, j, k\pm 1}^n = \pm \mathbf{e}_z \cdot \mathbf{Tf} \mathbf{r}_p^n \frac{N_s q_s}{2\Delta z} \quad (17c)$$

Here, the cell dimension is  $\Delta x \times \Delta y \times \Delta z$ . The current density through the surrounding

cell walls follows directly from charge conservation:

$$\mathbf{e}_x \cdot \langle \mathbf{j} \rangle_{i \pm \frac{1}{2}, j, k}^{n+\frac{1}{2}} = \pm \left( \langle \eta \rangle_{i \pm 1, j, k}^{n+1} - \langle \eta \rangle_{i \pm 1, j, k}^n \right) \frac{\Delta x}{\Delta t} \quad (18a)$$

$$\mathbf{e}_y \cdot \langle \mathbf{j} \rangle_{i, j \pm \frac{1}{2}, k}^{n+\frac{1}{2}} = \pm \left( \langle \eta \rangle_{i, j \pm 1, k}^{n+1} - \langle \eta \rangle_{i, j \pm 1, k}^n \right) \frac{\Delta y}{\Delta t} \quad (18b)$$

$$\mathbf{e}_z \cdot \langle \mathbf{j} \rangle_{i, j, k \pm \frac{1}{2}}^{n+\frac{1}{2}} = \pm \left( \langle \eta \rangle_{i, j, k \pm 1}^{n+1} - \langle \eta \rangle_{i, j, k \pm 1}^n \right) \frac{\Delta z}{\Delta t} \quad (18c)$$

Note that the above expressions are particular to the choice of quadratic weighting. This choice provides adequate smoothing, while also allowing for abrupt vacuum-dielectric transitions. A useful fact is that the current density due to an effective particle, through any cell wall enclosing that particle, is the normal component of  $\frac{1}{2}N_s q_s \mathbf{v}_p$ , where

$$\mathbf{v}_p = \text{Tf} \left( \frac{\mathbf{r}_p^{n+1} - \mathbf{r}_p^n}{\Delta t} \right) \quad (19)$$

is the velocity of the effective particle in the  $(\mathbf{e}_x, \mathbf{e}_y, \mathbf{e}_z)$  basis.

## B. Linear Stability and Accuracy

In an ordinary PIC code, the primary stability criterion is the Courant condition, which in one dimension reads  $c\Delta t < \Delta z$ , where  $\Delta t$  is the time step and  $\Delta z$  is the grid spacing. It is clear that in the presence of a dispersionless dielectric, this would be modified to read  $c\Delta t/n < \Delta z$ , where  $n$  is the refractive index. In the case of a fully dispersive model such as the one described above, the modification of the Courant condition is more subtle. Expressing Eqs. (6) and (7) in finite difference form, assuming propagation along a principal axis, and inserting exponential forms for  $A_i$  and  $\langle r_{is} \rangle$ , gives the numerical dispersion relation

$$\cos \omega \Delta t = \mathcal{V}(\mathbf{k}) + \mathcal{P}_i(\omega) \quad (20)$$

where

$$\mathcal{V}(\mathbf{k}) = 1 - 2c^2 \Delta t^2 \left( \frac{\sin^2 \frac{1}{2} k_x \Delta x}{\Delta x^2} + \frac{\sin^2 \frac{1}{2} k_y \Delta y}{\Delta y^2} + \frac{\sin^2 \frac{1}{2} k_z \Delta z}{\Delta z^2} \right) \quad (21)$$

and

$$\mathcal{P}_i(\omega) = \sum_s \frac{\frac{1}{2} f_{iis} \omega_{ps}^2 \Delta t^2 \sin^2 \frac{1}{2} \omega \Delta t}{\frac{1}{4} (\Omega^2)_{iis} \Delta t^2 - (1 + \Gamma_{iis} \Delta t) \sin^2 \frac{1}{2} \omega \Delta t - \frac{i}{2} \Gamma_{iis} \Delta t \sin \omega \Delta t} \quad (22)$$

Note that when the density of oscillators vanishes,  $\mathcal{P}_i \rightarrow 0$  and the well known vacuum equation is recovered. The effect of  $\mathcal{P}_i$  can be estimated by assuming  $\Omega^2 \Delta t^2 \ll 1$  and

$k_x \Delta x \sim k_y \Delta y \sim k_z \Delta z \sim \omega \Delta t \sim \pi$ . These assumptions are motivated by the fact that the resonance frequency should be well resolved, and by the expectation that numerical instabilities are most severe at the Nyquist frequency. Under these assumptions, the stability criterion becomes

$$\Delta t \lesssim \left( \frac{c^2}{\Delta x^2} + \frac{c^2}{\Delta y^2} + \frac{c^2}{\Delta z^2} \right)^{-1/2} \left( 1 - \frac{1}{4} \sum_s \frac{f_{is} \omega_{ps}^2 \Delta t^2}{1 + \Gamma_{is} \Delta t} \right)^{1/2} \quad (23)$$

This is more stringent than the usual Courant condition. Numerical experiments show that Eq. (23) is accurate in practice.

In order to evaluate the accuracy and stability of the differencing scheme more precisely, the numerical dispersion relation is evaluated numerically for the case of a single, lossless oscillator species. Since the dispersion relation scales, we normalize all frequencies to the resonant frequency,  $\Omega$ , taking  $\omega_p = 2\Omega$ ,  $\Delta z = 0.5c/\Omega$ , and  $\Delta x = \Delta y \rightarrow \infty$ . The results are shown in Fig. 3 for three choices of the time step. The case  $\Delta t = 0.2/\Omega$  is shown in panel (a), the case  $\Delta t = 0.4/\Omega$  is shown in panel (b), and the case  $\Delta t = 0.48/\Omega$  is shown in panel (c). The analytical dispersion relation is overlayed for comparison. As usual, the best accuracy is obtained for small values of  $\omega$  and  $k$ . As  $c\Delta t/\Delta z$  increases, the accuracy improves, until numerical instability sets in. This behavior is similar to the vacuum case. However, unlike the vacuum case, instability occurs for  $c\Delta t/\Delta z < 1$ , as shown in panel (c). Better accuracy may be obtained by decreasing both  $\Delta z$  and  $\Delta t$  proportionately.

### C. Nonlinear Stability

In the case of the fully nonlinear system, a rigorous stability analysis is difficult. However, if the oscillator equation is viewed as describing an effective particle in a potential well, the stability criterion may be viewed as the requirement that the particle never enter any region of runaway acceleration. Such a region exists if  $b > 0$ , for in this case there is a divergent repulsive force as  $r \rightarrow \pm\infty$ . Instability is also possible if  $b = 0$  and  $\mathbf{a} \neq 0$ . Assuming there are no metastable regions, the stability criterion can be written

$$\mathbf{F}_{\text{NL}} \cdot \mathbf{r} < m\Omega^2 \mathbf{r} \cdot \mathbf{r} \quad (24)$$

where

$$\mathbf{F}_{\text{NL}} = mb(\mathbf{r} \cdot \mathbf{r})\mathbf{r} - m\mathbf{a}\mathbf{r}\mathbf{r} \quad (25)$$

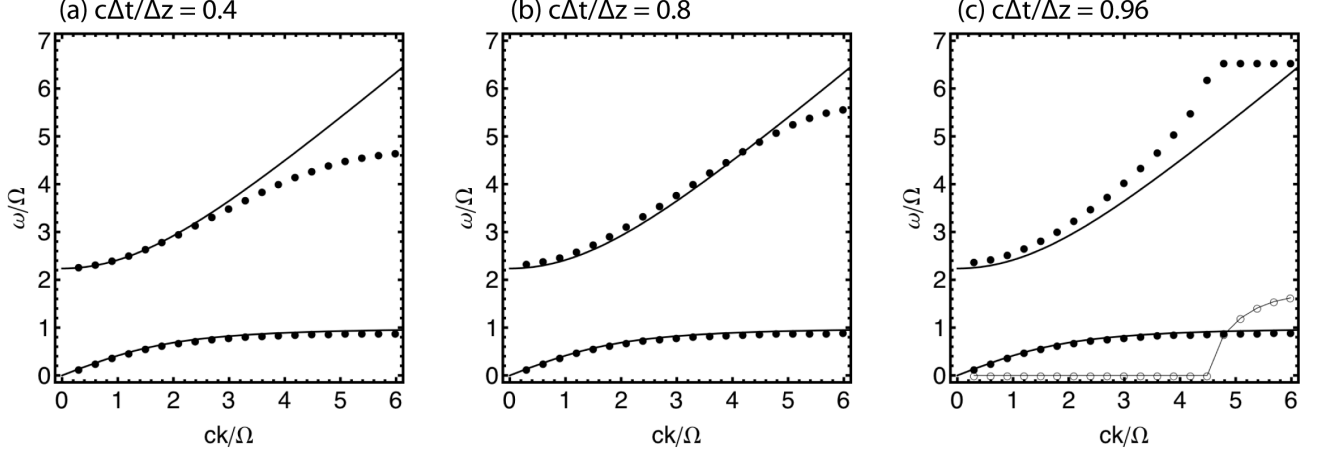


FIG. 3: Numerical dispersion for (a)  $c\Delta t/\Delta z = 0.4$ , (b)  $c\Delta t/\Delta z = 0.8$ , and (c)  $c\Delta t/\Delta z = 0.96$ . Solid curves are the analytical dispersion relation, solid circles are  $\Re(\omega/\Omega)$ , and open circles connected by a thin line are  $\Im(\omega/\Omega)$ . In all cases,  $\omega_p/\Omega = 2$ , and  $\Delta z = 0.5c/\Omega$ . Panel (c) shows that numerical instability may occur for  $c\Delta t/\Delta z < 1$ .

If one is interested primarily in second order effects, the system can be stabilized by taking  $b < 0$ . The magnitude of  $b$  is chosen such that the order of magnitude of the first, second, and third order forces are the same at some critical point. This leads to

$$b \approx -\frac{a^2}{\Omega^2} \quad (26)$$

where  $a$  and  $\Omega$  are typical values of the elements of  $\mathbf{a}$  and  $\Omega$ . If third order effects are important physically, a stabilizing fifth order nonlinearity can be easily introduced. In this case,

$$\mathbf{F}_{\text{NL}} = md(\mathbf{r} \cdot \mathbf{r})^2 \mathbf{r} + mb(\mathbf{r} \cdot \mathbf{r}) \mathbf{r} - m\mathbf{a}rr \quad (27)$$

where  $d$  is the fifth order anharmonic coefficient. Demanding that the first, third, and fifth order forces be equal at some critical point gives

$$d \approx -\frac{b^2}{\Omega^2} \quad (28)$$

The ultimate nonlinear stabilization technique would utilize physical effects, such as ionization in the case of the electronic oscillator, or material damage in the case of the lattice oscillator. However, accounting for these processes is beyond the scope of the present work.

Parameter	Lattice Oscillator	False Resonance
Oscillator Strength, $f$	1	1
Resonance Frequency, $\Omega$	$6.90 \times 10^{13}$ rad/s	$8.91 \times 10^{14}$ rad/s
Damping Frequency, $\Gamma$	$6.25 \times 10^{10}$ rad/s	0
Plasma Frequency, $\omega_p$	$9.27 \times 10^{13}$ rad/s	$2.46 \times 10^{15}$ rad/s
Anharmonic Coefficient, $a_{123}$	$-3.28 \times 10^{37} \text{ m}^{-1}\text{s}^{-2}$	$1.23 \times 10^{40} \text{ m}^{-1}\text{s}^{-2}$

TABLE II: False Resonance Model for Gallium Phosphide

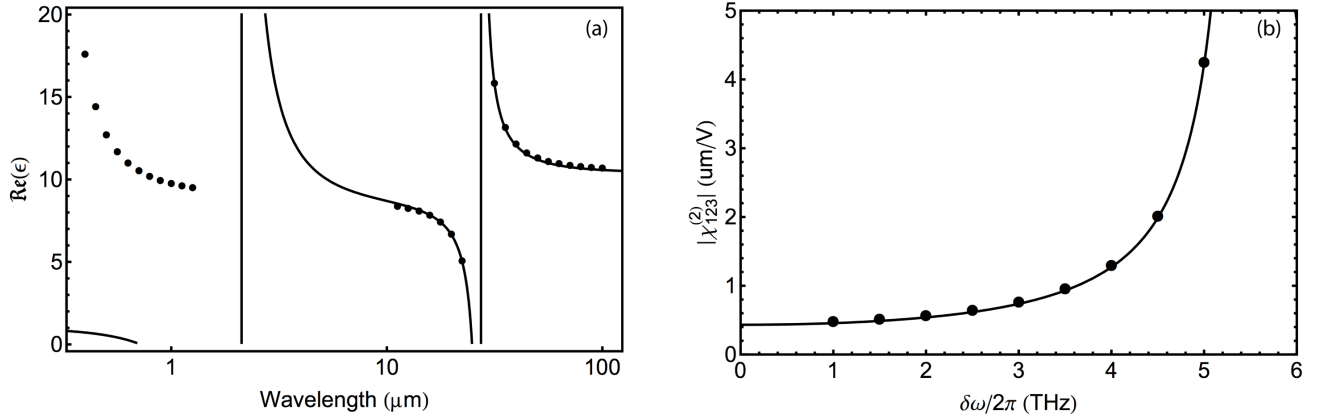


FIG. 4: False resonance model for GaP. Panel (a) displays  $\Re(\epsilon)$ , where the solid curve is the false resonance model and the points are from the expressions in Ref. [21]. Panel (b) displays  $\chi_{123}^{(2)}(2\delta\omega, \delta\omega, \delta\omega)$ , where the curve is the false resonance model and the points are the true resonance model (Table I).

#### D. False Resonance Technique for Accelerating Computation

It sometimes happens that the accuracy and stability criteria,  $\Omega^2 \Delta t^2 \ll 1$  and  $\omega_p^2 \Delta t^2 \ll 1$ , force one to use a very large number of time steps to simulate a given process. This limitation can be mitigated if the frequency range of interest is well below  $\Omega$ . In such cases, it is possible to artificially shift  $\Omega$  to a lower frequency while preserving the dispersion relation in the region of interest. In this way, the “true resonance” is replaced by a “false resonance” which is easier to resolve, but leads to the same physics.

As an example of a false resonance model, consider again GaP, which has the true resonance parameters displayed in Table I. When modeling an electron bunch with a characteristic time of, say, 100 femtoseconds, the frequency range of interest is well below the electronic



resonance, which has  $2\pi/\Omega \approx 1$  femtosecond. One may then use a false resonance model such as the one described by Table II. The linear and nonlinear dispersion curves associated with this model are shown in Fig. 4. In the THz range, the dispersion relation remains accurate. Note that the dispersion in this range could be fine tuned by adding additional false resonances.

### E. Boundary Conditions and Moving Window

In simulations of laser-plasma interactions, the moving window technique [31] is often used. In this technique, the mesh points are shifted by one cell in between time levels such that the computational region, or “window,” moves at the speed of light. Boundary conditions are greatly simplified by the requirements of causality. When the plasma density is low, the laser pulse group velocity is nearly the speed of light, and the pulse stays in the window for a long time. Hence, the window only has to be as long as the laser pulse, even if the interaction region is much longer.

When the group velocity is significantly smaller than the speed of light, the pulse quickly falls behind a light frame window, and one might as well work in the lab frame. If the window speed is the group velocity, a fully dispersive model might allow precursor signals to reach the front of the window. Moreover, signals reflected from the back of the window might work their way toward the region of interest. One solution is to use perfectly matched layers (PML) [32] to absorb waves near the boundaries of the window. In order for this to be effective, it is necessary to use a large number of layers due to the fact that the moving window involves shifting the field data by one cell between time levels. In order that this shift should weakly perturb the solution, the PML conductivity has to change very gradually from one cell to the next.

In the case of lab frame simulations, another option is to use Lindman’s absorbing boundary condition [33] in the longitudinal direction, and periodic boundary conditions transversely. If a Poisson equation has to be solved, the solution in the box can be matched to a decaying solution outside the box [30].

## VI. NUMERICAL EXPERIMENTS

The model described above has been implemented as a module within the turboWAVE [3] framework. In this section, three numerical experiments are presented. First, the electro-optic effect in GaP is demonstrated by comparing the numerical change in polarization with that predicted by the low frequency theory. Second, soliton propagation in fused silica is demonstrated. Finally, to take full advantage of the PIC framework, a relativistic electron bunch is passed near a GaP crystal, and the induced fields are examined.

### A. Electro-Optic Effect

In this numerical experiment, an  $x$ -polarized laser pulse is copropagated with a  $y$ -polarized THz half-wave in a GaP crystal, and the change in the polarization state of the laser pulse is measured. The length of the THz half-wave is chosen to be long enough so that the standard picture of the electro-optic effect applies. In this picture, the change in the impermeability [38] tensor due to a DC electric field is

$$\Delta\eta_{ij} = r_{ijk}E_k \quad (29)$$

For any Zinc-Blende type crystal,  $r_{ijk} = r_{123} = r_{41}$  if all three indices are distinct, and  $r_{ijk} = 0$  otherwise. The crystal orientation is represented by the operator  $\mathsf{T}$ , which can be viewed as a sequence of rotations that re-orient the crystal starting with the  $(\mathbf{e}_u, \mathbf{e}_v, \mathbf{e}_w)$  and  $(\mathbf{e}_x, \mathbf{e}_y, \mathbf{e}_z)$  bases aligned. It turns out that the electro-optic effect is maximized if [34]

$$\mathsf{T} = R_z(\pi/2)R_x(-\pi/2)R_z(\pi/4) \quad (30)$$

with the laser field polarized in the  $x$ -direction and the DC field polarized in the  $y$ -direction. Here,  $R_i$  is an active right-handed rotation about the  $i^{\text{th}}$  coordinate axis. As an example, if  $E$  and  $\Delta\eta$  are given in the  $(\mathbf{e}_x, \mathbf{e}_y, \mathbf{e}_z)$  basis, and  $\mathbf{r}$  is given in the  $(\mathbf{e}_u, \mathbf{e}_v, \mathbf{e}_w)$  basis, then  $\Delta\eta = \mathsf{Tr}\mathsf{T}^{-1}\mathbf{E}\mathsf{T}^{-1}$ . To calculate the change in polarization due to the electro-optic effect, a principal axis transformation is usually made [34]. Alternatively, one may make direct use of the solution of the slowly varying envelope equation,

$$\mathcal{E}(z) = \exp\left(\frac{i\pi\Delta\epsilon z}{n\lambda_0}\right)\mathcal{E}(z=0) \quad (31)$$

where  $\mathcal{E}$  is the complex electric field envelope,  $\lambda_0$  is the free space laser wavelength,  $n$  is the refractive index of the unperturbed crystal, and  $\Delta\epsilon$  is the change in permittivity induced by the DC field. This equation remains valid even when  $\Delta\epsilon$  is a tensor and  $\mathcal{E}$  is a vector, and is easily evaluated in a software environment that supports the exponential of a matrix.

We now compare the prediction of Eq. (31) with the results of a turboWAVE simulation. In the simulation, an  $x$ -polarized laser pulse and a  $y$ -polarized THz half-wave are incident on a GaP crystal oriented as in Eq. (30). The simulation parameters are given in Tables I and III. The lattice nonlinearity was stabilized with  $b = -a^2/\Omega^2$ . The results from the simulation are shown in Fig. 5. The data are evaluated 60  $\mu\text{m}$  into the crystal to avoid interference from reflections generated at either vacuum-crystal interface. Since the turboWAVE model uses a universal electric field, the optical and THz frequency components have to be extracted by means of a Fourier filter. The envelope of the optical wave is constructed by applying a hard-edged band-pass filter centered at the optical frequency,  $+\omega_0$ . The result is then shifted in frequency by  $-\omega_0$ , multiplied by 2 (to account for the energy in the negative frequencies) and the inverse Fourier transform is applied. Based on Fig. 5, the polarization ratio at  $z = 60 \mu\text{m}$ , and at times prior to the generation of internal reflections, is  $|\mathcal{E}_y/\mathcal{E}_x|^2 \approx 0.0018$ . Applying the analytical formula with the inputs  $E_y = 68 \text{ kV/cm}$ ,  $n = 3.16$ , and  $r_{123} = 0.89 \text{ pm/V}$  gives  $|\mathcal{E}_y/\mathcal{E}_x|^2 \approx 0.0019$ . Thus, the simulation model closely agrees with the theoretical prediction.

An interesting feature of the simulation data is that the second  $y$ -polarized optical pulse is larger than the first. This appears to happen because the reflected  $x$ -polarized optical pulse continues to be rotated by the reflected  $y$ -polarized THz pulse. This leads to a coherent reinforcement of the reflected  $y$ -polarized optical pulse.

## B. Soliton Propagation

In this numerical experiment, a 20 femtosecond, 2.1  $\mu\text{m}$  pulse is propagated in fused silica in both the linear and soliton regimes. The Sellmeier formula for fused silica can be matched exactly to a three oscillator model, the parameters of which are displayed in Table IV. The second anharmonic coefficient is chosen to give a nonlinear refractive index of  $n_2 = 3 \times 10^{-16} \text{ cm}^2/\text{W}$ . The choice to take  $b \neq 0$  only in the third oscillator has no effect other than on the frequency dependence of  $n_2$ .

Parameter	Symbol	Value
Time Step	$c\Delta t$	$0.012 \mu\text{m}$
Space Step	$\Delta z$	$0.017 \mu\text{m}$
Cells	$N_z$	$2^{13}$
Steps	$N_t$	$2^{17}$
THz Field	$E_y$	$68 \text{ kV/cm}$
THz Half Wave	$\tau_H$	$2.2 \text{ ps}$
Laser Field	$ \mathcal{E}_x $	$18 \text{ kV/cm}$
Laser FWHM	$\tau_L$	$220 \text{ fs}$
Laser wavelength	$\lambda_0$	$0.81 \mu\text{m}$
Crystal Length	$L$	$120 \mu\text{m}$
Crystal Orientation	$\mathsf{T}$	Eq. 30

TABLE III: Parameters for simulation of electro-optic effect. The fields are measured inside the dielectric. The THz field is a half-cycle pulse with base-to-base width  $\tau_H$ .

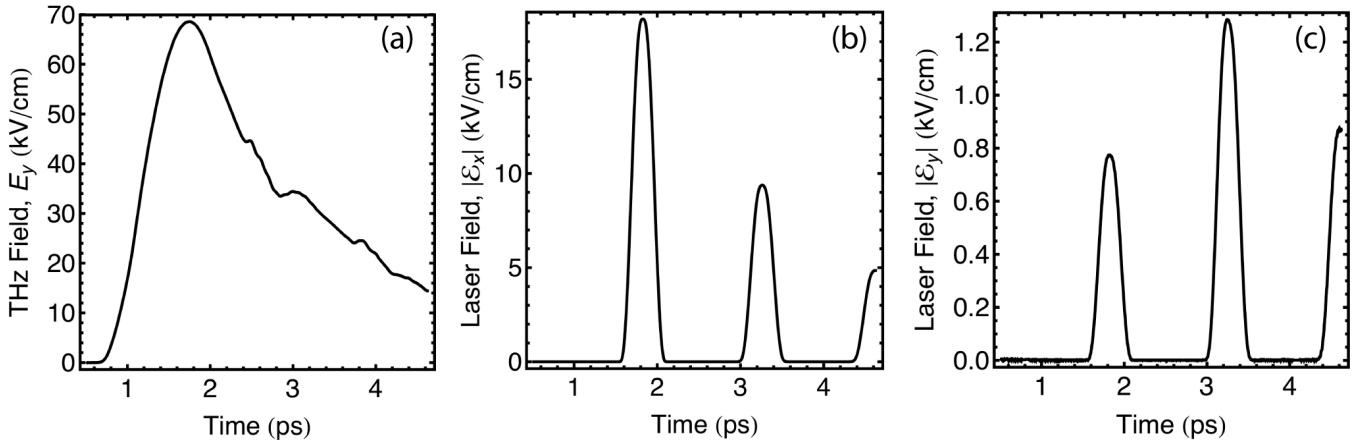


FIG. 5: Simulated electric field vs. time at  $z = 60 \mu\text{m}$  from the entrance plane of the crystal. (a)  $y$ -polarized THz field (low-pass Fourier filter) (b)  $x$ -polarized optical field envelope (band-pass Fourier filter with shift) (c)  $y$ -polarized optical field envelope (band-pass Fourier filter with shift). The incident optical field is a single, purely  $x$ -polarized pulse, and the incident THz field is a single, purely  $y$ -polarized half-wave. The additional optical pulses, and the late-time distortion of the THz field, are due to reflections.

Parameter	Osc. 1	Osc. 2	Osc. 3	Unit
Oscillator Strength, $f$	1	1	1	
Resonance Frequency, $\Omega$	$2.35 \times 10^{14}$	$1.63 \times 10^{16}$	$2.78 \times 10^{16}$	rad/s
Damping Frequency, $\Gamma$	0	0	0	rad/s
Plasma Frequency, $\omega_p$	$1.79 \times 10^{14}$	$1.06 \times 10^{16}$	$2.30 \times 10^{16}$	rad/s
Anharmonic Coefficient, $b$	0	0	$4.72 \times 10^{54}$	$\text{m}^{-2}\text{s}^{-2}$

TABLE IV: Oscillator Parameters for Fused Silica

Parameter	Symbol	Value
Time Step	$c\Delta t$	$0.014 \mu\text{m}$
Space Step	$\Delta z$	$0.034 \mu\text{m}$
Cells	$N_z$	$2^{12}$
Steps	$N_t$	$4 \times 10^5$
Window Speed	$v_g$	$0.68c$
PML thickness	-	$8.7 \mu\text{m}$
Intensity	$I_0$	$0.4 \text{ TW}/\text{cm}^2$
Pulse Width	$T_0$	$20 \text{ fs}$
Free Space Wavelength	$\lambda_0$	$2.1 \mu\text{m}$
Dispersion Length	$L_D$	$2.8 \text{ mm}$
Nonlinear Length	$L_{NL}$	$2.8 \text{ mm}$
GVD Coefficient	$\beta_2$	$-1.42 \times 10^{-25} \text{ s}^2/\text{m}$

TABLE V: Parameters for simulation of soliton propagation.

The amplitude envelope of the fundamental soliton has the form  $\text{sech}(\tau)$ , where  $\tau = (t - z/v_g)/T_0$ ,  $v_g$  is the group velocity, and  $T_0$  is the pulse width parameter. In simulations, it is convenient to have a function whose support is strictly in a finite region. Furthermore, in a model of the type used here, the initial conditions depend on  $z$ , and the pulse starts in vacuum. Hence, the appropriate initial condition is [39]

$$E_x(t = 0, z) = \epsilon^{1/4} |\mathcal{E}_0| \text{sech}(\zeta/cT_0) \sin(\omega_0 \zeta/c) C(\zeta/cT_0) \quad (32)$$

where  $\zeta = z - z_0$ ,  $z_0$  fixes the spatial origin, and  $C(x)$  is a suitable clipping function. The

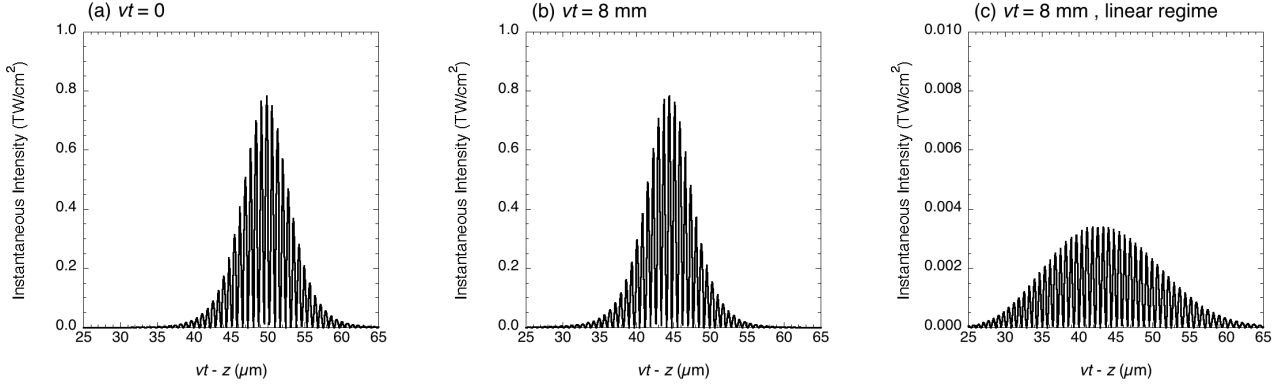


FIG. 6: Simulation of 1D soliton propagation in fused silica. Plots show  $\epsilon^{1/2}E_x^2/\eta_0$  vs.  $v_g t - z$ , where  $v_g t$  is held fixed in each plot, and  $v_g$  is the velocity of the moving window. Panel (a) shows the initial pulse, (b) shows the pulse after 8 mm propagation, and (c) shows the result from (b) in the case where the initial intensity is  $I_0/100$ .

clipping function used here is

$$C(x) = \begin{cases} |x| \leq 4 & , 1 \\ 4 < |x| < 6 & , \cos^2[(|x| - 4)\pi/4] \\ |x| \geq 6 & , 0 \end{cases} \quad (33)$$

The parameters of the pulse, and the numerical parameters associated with the simulation, are displayed in Table V. The intensity and electric field are related by  $I_0 = \epsilon^{1/2}|\mathcal{E}_0|^2/2\eta_0$ . The free space wavelength is  $\lambda_0 = 2\pi c/\omega_0$ . The group velocity dispersion (GVD) coefficient is defined by  $c\beta_2 = \partial^2(\epsilon^{1/2}\omega)/\partial t^2|_{\omega=\omega_0}$ . The dispersion length,  $L_D = T_0^2/|\beta_2|$ , measures the propagation length needed to observe group velocity dispersion (GVD) effects. The nonlinear length,  $L_{NL} = c/\omega_0 n_2 I_0$ , measures the propagation length needed to observe nonlinear pulse distortions. The conditions  $\beta_2 < 0$  and  $L_D = L_{NL}$  result in stable propagation of the pulse without distortion [20, 35]. This is illustrated in Fig. 6. Comparison of panels (a) and (b) shows that when  $I_0 = 0.4$  TW/cm<sup>2</sup>, the pulse maintains its original form after propagating nearly  $3L_D$ . Panel (c) shows that when  $I_0$  is reduced by a factor of 100, the pulse broadens significantly over the same propagation distance.

Parameter	Symbol	Value
Time Step	$c\Delta t$	0.168 $\mu\text{m}$
Space Step	$\Delta x = \Delta y = \Delta z$	0.672 $\mu\text{m}$
Cells	$N_x \times N_y \times N_z$	$2^{10} \times 2^{10} \times 2^{10}$
Steps	$N_t$	$3 \times 10^4$
Window Speed	$v$	$c$
Bunch Diameter	$r_b$	8 $\mu\text{m}$
Bunch Length	$\tau_b$	80 fs
Electron Energy	$(\gamma - 1)mc^2$	250 MeV
Crystal Size	$L_x \times L_y \times L_z$	$605 \times 360 \times \infty \mu\text{m}^3$
Crystal Orientation	T	Eq. 30

TABLE VI: Parameters for simulation of fields induced by an electron bunch.

### C. Electron Bunch Passing Near a Crystal

A three dimensional simulation of the fields generated in an electro-optic crystal by a passing relativistic electron bunch was described in Ref. [17]. Here, a similar simulation is carried out, with the following distinctions. First, the bunch charge is varied until significant nonlinear distortions are observed in the bunch fields. Second, the false resonance technique is used to accelerate the calculation, rather than the sub-cycling technique that was used in Ref. [17]. The former technique is found to have superior stability and conservation properties. The false resonance oscillator parameters are the same as those given in Table II, except that a stabilizing third order nonlinearity is added to each oscillator. The other parameters of the simulation are given in Table VI.

Figs. 7(a) and (b) display the electric field component  $E_y(x = 0, y, z)$ , for the cases  $Q = 0.28$  pC and  $Q = 2.8$  pC, where  $Q$  is the bunch charge. Figs. 7(c) and (d) show the corresponding line-outs at  $y = 0$ . The bunch charge affects the degree of nonlinearity in the interaction. The primary features are the vertical phase fronts located in the range  $-400 < z - ct < -300 \mu\text{m}$ , and the diagonal phase front that appears at all  $z - ct$ . As discussed previously [17], these can be roughly associated with coherent transition radiation (CTR) and Cherenkov radiation, respectively. In electro-optic sensing applications, the

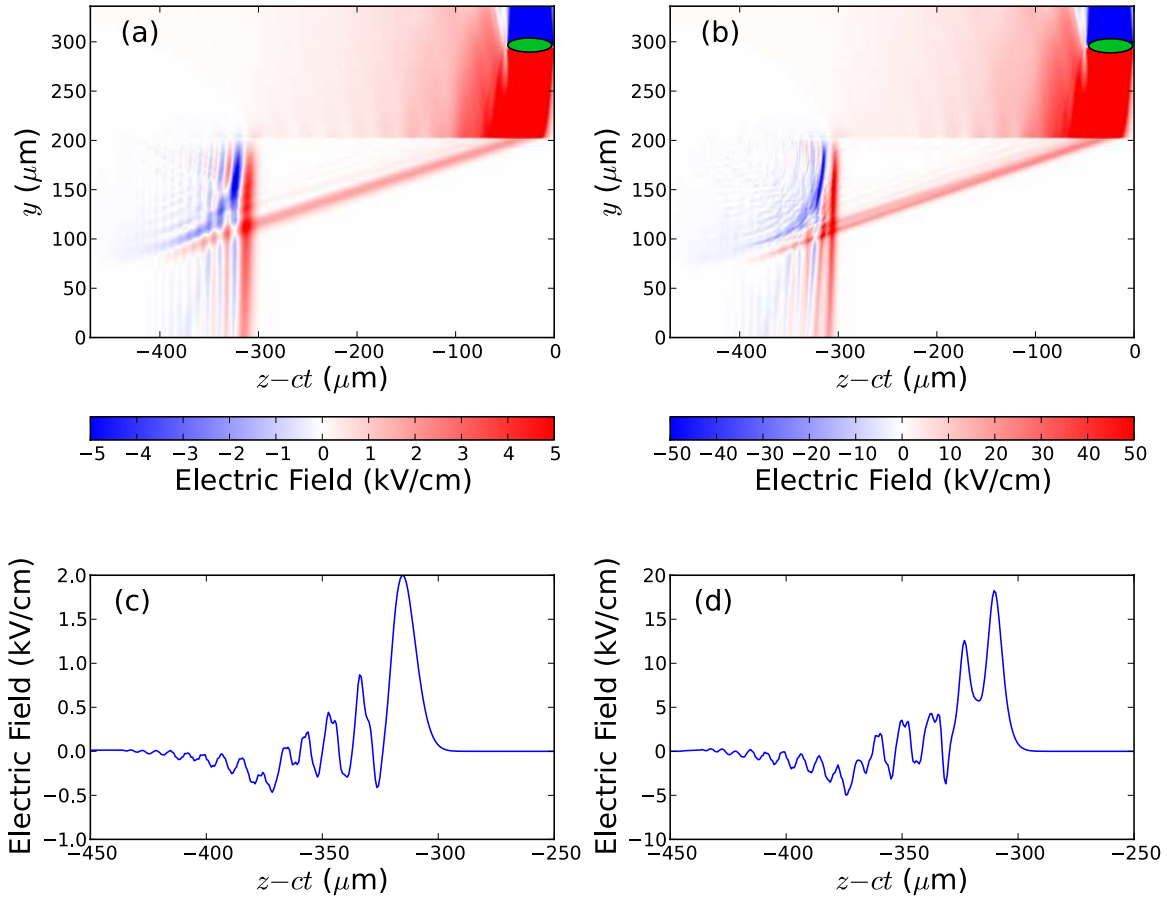


FIG. 7: Simulation of fields induced by an electron bunch with (a,c)  $Q = 0.28$  pC and (b,d)  $Q = 2.8$  pC. The three dimensional data is evaluated at  $x = 0$  in order to present a two dimensional plot. The green oval represents the location of the electron bunch, which propagates from left to right. The boundary between the crystal and vacuum is located at  $y = 200 \mu\text{m}$ . The plane of incidence is located at  $z - ct = -435 \mu\text{m}$ . The line-outs in (c) and (d) are evaluated at  $y = 0$ .

CTR-like feature is supposed to retain the form of the vacuum bunch fields. However, as is well known, dispersive effects lead to distortions of the type shown in the figure.

When the bunch charge is high enough to excite large nonlinear polarization currents in the material, the fields induced in the crystal may be further distorted. Such a case is shown



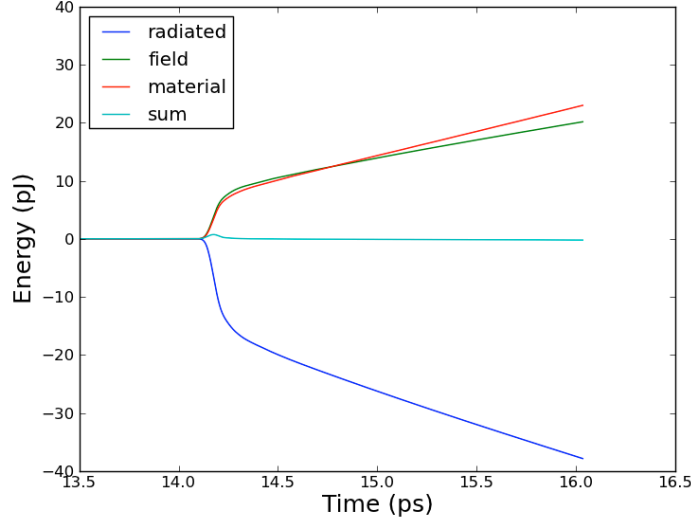


FIG. 8: Conservation of energy during simulated bunch-crystal interaction.

in Figs. 7(b) and (d). For the chosen crystal orientation, the nonlinear polarization is

$$\mathbf{P}^{(2)} = \chi_{123}^{(2)} E_y^2 \mathbf{e}_x + 2\chi_{123}^{(2)} E_x E_y \mathbf{e}_y \quad (34)$$

Hence, a  $y$ -polarized THz field induces an  $x$ -polarized field with second harmonic components. This field then mixes with the original  $y$ -polarized field to produce a distorted  $y$ -polarized field. This distortion can be clearly seen by comparing panels (c) and (d) of Fig. 7. Qualitatively, the effect is to produce narrower features in the waveform. In an electro-optic sensing application, this could adversely affect the fidelity of the diagnostic.

Finally, consider the flow of energy in the crystal during the simulation. For the specific form of the dielectric response considered in this report, Poynting's theorem can be written as

$$\int_{\partial\Omega} d\mathbf{n} \cdot \mathbf{S} + \frac{\epsilon_0}{2} \frac{d}{dt} \int_{\Omega} d^3\mathbf{r} (E^2 + c^2 B^2) + \sum_{p \in \Omega} \left( \frac{dU_p}{dt} + \mathcal{L}_p \right) = 0 \quad (35)$$

where the first term is the energy radiated through a surface  $\partial\Omega$ , the second is the rate of change of field energy in the volume  $\Omega$ , and the third is the rate of change of the energy of all the effective particles in  $\Omega$ . Here, the effective particle energy is

$$U_p = \frac{1}{2} m_p \left( \frac{dr_p}{dt} \right)^2 + q_p \phi_p(r_p) \quad (36)$$

where  $m_p$  is the mass,  $r_p$  is the displacement,  $q_p$  is the charge, and  $\phi_p(r_p)$  is the microscopic electrostatic potential of the displaced particle. The rate of frictional damping for an effective

particle is

$$\mathcal{L}_p = 2\Gamma_p m_p \left( \frac{dr_p}{dt} \right)^2 \quad (37)$$

Fig. 8 displays the three terms in Poynting’s theorem, integrated over time, along with the sum. The “radiated” curve is negative, corresponding to the fact that the bunch fields propagate into the crystal. The steep initial slope corresponds to the generation of the CTR-like feature, while the more gradual slope corresponds to the generation of the Cherenkov-like feature. The “field” and “material” curves show that half the incident energy goes to the fields, while the other half goes to the effective particles. The “sum” curve shows that energy is conserved, to the extent that it vanishes. One notices a slight discrepancy at the moment the bunch fields first enter the crystal. This may be related to the numerical process of generating a reflected wave.

## VII. CONCLUSIONS

The physics of nonlinear crystals excited by laser pulses, plasmas, particle beams, or any combination of these, can be numerically simulated using an effective particle model based on particle-in-cell techniques. In this model, bound charges respond to a superposition of microscopic and macroscopic fields, where the former are chosen to satisfy the known dispersion characteristics of the material, and the latter are self-consistently computed using the usual FDTD technique. The resulting numerical model is extremely flexible and makes very few assumptions. It is, however, computationally expensive. Nevertheless, it is now possible to carry out three dimensional simulations of electro-optic sensing, where the bunch fields induced in an electro-optic crystal are computed with unprecedented detail. Other applications of this model might include modeling the nonlinear optics of nano-composites, or frequency mixing with ultra-short pulses.

## VIII. ACKNOWLEDGEMENTS

This work was supported by NRL Base Funds and the Department of Energy. We acknowledge useful conversations with B. Hafizi and A. Ting.

- 
- [1] K. Yee, Numerical solution of initial boundary value problems involving Maxwell's equations in isotropic media, *IEEE Trans. Antennas Propagat.* 14 (1966) 302.
  - [2] J. P. Verboncoeur, particle simulation of plasmas: review and advances, *Plasma Phys. and Control. Fusion* 47 (2005) A231–A260.
  - [3] D. Gordon, Improved ponderomotive guiding center algorithm, *IEEE Trans. Plasma Sci.* 35 (2007) 1486–1488.
  - [4] D. W. Forslund, J. M. Kindel, E. L. Lindman, Plasma simulation studies of stimulated scattering processes in laser-irradiated plasmas, *Phys. Fluids* 18 (1975) 1017–1030.
  - [5] C. D. Decker, W. B. Mori, T. Katsouleas, Particle-in-cell simulations of raman forward scattering from short-pulse high-intensity lasers, *Phys. Rev. E* 50 (1994) 3338.
  - [6] P. Mora, T. Antonsen, Kinetic modeling of intense, short laser pulses propagating in tenuous plasmas, *Phys. Plasmas* 4 (1997) 217.
  - [7] A. Pukhov, J. Meyer-ter-Vehn, Relativistic laser-plasma interaction by multi-dimensional particle-in-cell simulations, *Phys. Plasmas* 5 (1998) 1880–1886.
  - [8] R. Fonseca, L. Silva, F. Tsung, V. Decyk, W. Lu, C. Ren, W. Mori, S. Deng, S. Lee, T. Katsouleas, J. Adam, OSIRIS: a three dimensional, fully relativistic particle in cell code for modeling plasma based accelerators, *Lect. Notes Comput. Sci.* 2331 (2002) 342–351.
  - [9] C. Nieter, J. Cary, VORPAL: a versatile plasma simulation code, *J. Comp. Phys.* 196 (2004) 448–473.
  - [10] C. Huang, V. Decyk, C. Ren, M. Zhou, W. Lu, W. Mori, J. Cooley, T. Antonsen, T. Katsouleas, QUICKPIC: a highly efficient particle-in-cell code for modeling wakefield acceleration in plasmas, *J. Comp. Phys.* 217 (2006) 658–79.
  - [11] M. Mlejnek, E. Wright, J. Moloney, Dynamic spatial replenishment of femtosecond pulses propagating in air, *Opt. Lett.* 23 (1998) 382–384.
  - [12] J. Peñano, P. Sprangle, B. Hafizi, A. Ting, D. Gordon, C. Kapetanakis, Propagation of ultra-short, intense laser pulses in air, *Phys. Plasmas* 11 (2004) 2865–2874.
  - [13] M. Fujii, M. Tahara, I. Sakagami, W. Freude, P. Russer, High-order FDTD and auxiliary differential equation formulation of optical pulse propagation in two-dimensional kerr and raman nonlinear dispersive media, *IEEE J. Quantum Electron.* 40 (2004) 175–182.

- [14] J. Peñano, P. Sprangle, B. Hafizi, W. Manheimer, A. Zigler, Transmission of intense femtosecond laser pulses into dielectrics, *Phys. Rev. E* 72 (2005) 36412–1–7.
- [15] J. Greene, A. Taflove, General vector auxiliary differential equation finite-difference time-domain method for nonlinear optics, *Opt. Exp.* 14 (2006) 8305–8310.
- [16] S. Champeaux, L. Berge, D. Gordon, A. Ting, J. Peñano, P. Sprangle, (3+1)-dimensional numerical simulations of femtosecond laser filaments in air : toward a quantitative agreement with experiments, *Phys. Rev. E* 77 (2008).
- [17] D. Gordon, M. Helle, D. Kaganovich, A. Ting, Electro-optic and terahertz diagnostics, in: S. Gold, G. Nusinovich (Eds.), *AIP Conf. Proc.* no. 1299, pp. 67–75.
- [18] M. Helle, D. Gordon, D. Kaganovich, A. Ting, Extending electro-optic detection to ultrashort electron beams, *Phys. Rev. ST/AB* 15 (2012) 052801–1–052801–11.
- [19] J. Jackson, *Classical Electrodynamics*, John Wiley and Sons, New York, 1975.
- [20] R. Boyd, *Nonlinear Optics*, Academic Press, San Diego, second edition, 2003.
- [21] S. Casalbuoni, H. Schlarb, B. Schmidt, P. Schmuser, B. Steffen, A. Winter, Numerical studies on the electro-optic detection of femtosecond electron bunches, *Phys. Rev. ST/AB* 11 (2008) 072802–1–072802–18.
- [22] W. Faust, C. Henry, R. Eick, Dispersion in the nonlinear susceptibility of GaP near the reststrahl band, *Phys. Rev.* 173 (1968) 781–786.
- [23] Y. Berozashvili, S. Machavariani, A. Natsvlishvili, A. Chirakadze, Dispersion of the linear electro-optic coefficients and the non-linear susceptibility in GaP, *J. Phys. D: Appl. Phys.* 22 (1988) 682–686.
- [24] G. Gallot, D. Grischkowsky, Electro-optic detection of terahertz radiation, *J. Opt. Soc. Am. B* 16 (1999) 1204–1212.
- [25] S. Jamison, J. Shen, A. MacLeod, W. Gillespie, D. Jaroszynski, High-temporal-resolution, single-shot characterization of terahertz pulses, *Opt. Lett.* 28 (2003) 1710–1712.
- [26] G. Berden, S. Jamison, A. MacLeod, W. Gillespie, B. Redlich, A. van der Meer, Electro-optic technique with improved time resolution for real-time, nondestructive, single-shot measurements of femtosecond electron bunch profiles, *Phys. Rev. Lett.* 93 (2004) 114802–1–114802–4.
- [27] G. Berden, W. Gillespie, S. Jamison, E.-A. Knabbe, A. MacLeod, A. van der Meer, P. Phillips, H. Schlarb, B. Schmidt, P. Schmuser, B. Steffen, Benchmarking of electro-optic monitors for femtosecond electron bunches, *Phys. Rev. Lett.* 99 (2007) 164801–1–164801–4.

- [28] A. Debus, M. Bussmann, U. Schramm, R. Sauerbrey, C. Murphy, Z. Major, R. Horlein, L. Veisz, K. Schmid, J. Schreiber, K. Witte, S. Jamison, J. Gallacher, D. Jaroszynski, M. Kaluza, B. Hidding, S. Kiselev, R. Heathcote, P. Foster, D. Neely, E. Divall, C. Hooker, J. Smith, K. Ertel, A. Langley, P. Norreys, J. Collier, S. Karsch, Electron bunch length measurements from laser-accelerated electrons using single-shot THz time-domain interferometry, *Phys. Rev. Lett.* 104 (2010) 084802–1–084802–4.
- [29] T. Esirkepov, Exact charge conservation scheme for Particle-in-Cell simulation with an arbitrary form-factor, *Computer Phys. Comm.* 135 (2001) 144–153.
- [30] C. K. Birdsall, A. B. Langdon, *Plasma Physics via Computer Simulation*, Institute of Physics Publishing, Bristol and Philadelphia, 1991.
- [31] C. Decker, W. Mori, Group velocity of large amplitude electromagnetic waves in a plasma, *Phys. Rev. Lett.* 72 (1994) 490–493.
- [32] J.-P. Berenger, Three-dimensional perfectly matched layer for the absorption of electromagnetic waves, *J. Comp. Phys.* 127 (1996) 363–379.
- [33] E. Lindman, “free space” boundary conditions for the time dependent wave equation, *J. Comp. Phys.* 18 (1975) 66–78.
- [34] A. Yariv, P. Yeh, *Optical Waves in Crystals*, John Wiley and Sons, 2003.
- [35] G. Agrawal, *Nonlinear fiber optics, Optics and Photonics*, Academic Press, San Diego, second edition, 1995.
- [36] The coupling of free and bound charges is through the macroscopic field only, i.e., collisions are neglected. As a result, the model is most useful when the free charges do not impinge on the dielectric.
- [37] In the present work, we assume local phase coherence. By using many effective particles per cell, this assumption could be removed.
- [38] Impermeability is defined by  $\eta = \epsilon^{-1}$ , where  $\epsilon$  is the relative permittivity
- [39] Reflection losses occur in the simulation, but are neglected in Eq. (32).

## Appendix

In this appendix, the relationship between the nonlinear refractive index,  $n_2$ , and the second anharmonic coefficient,  $b$ , is derived. For simplicity, all quantities are reduced to scalars.

Consider a perturbation expansion of the anharmonic oscillator equation. Suppressing the species index, and expressing all quantities in frequency space, the first order equation is

$$\mathcal{D}(\omega)r^{(1)} = \frac{q}{m}E(\omega) \quad (38)$$

and the third order equation is

$$\mathcal{D}(\omega)r^{(3)} = b \left( r^{(1)} * r^{(1)} \right) * r^{(1)} \quad (39)$$

Here, the asterisk denotes convolution over frequency, and the electric field is in the form

$$E(\omega) = \frac{E_0}{2} [\delta(\omega - \omega_0) + \delta(\omega + \omega_0)] \quad (40)$$

Inserting  $r^{(1)}$  into the third order equation gives

$$r^{(3)} = b \left( \frac{qE_0}{2m} \right)^3 \frac{F(\omega)}{\mathcal{D}(\omega)} \quad (41)$$

where

$$F(\omega) = \frac{\delta(\omega - 3\omega_0)}{\mathcal{D}^3(\omega_0)} + \frac{3\delta(\omega - \omega_0)}{\mathcal{D}^2(\omega_0)\mathcal{D}(-\omega_0)} + \frac{3\delta(\omega + \omega_0)}{\mathcal{D}^2(-\omega_0)\mathcal{D}(\omega_0)} + \frac{\delta(\omega + 3\omega_0)}{\mathcal{D}^3(-\omega_0)} \quad (42)$$

Restoring species indices, the nonlinear polarization is

$$P^{(3)} = \sum_s N_s q_s r_s^{(3)} \quad (43)$$

This quantity must now be connected to the refractive index.

The refractive index is defined by  $n = \epsilon^{1/2}$ , with  $\epsilon$  the relative permittivity. Using  $D = \epsilon_0 \epsilon E$ , this can be written as

$$n = \left( \frac{\epsilon_0 E + P}{\epsilon_0 E} \right)^{1/2} \quad (44)$$

For a weakly nonlinear interaction,  $P^{(3)} \ll P^{(1)}$ , and

$$n \approx n_0 + \frac{P^{(3)}}{2n_0\epsilon_0 E} \quad (45)$$

where  $n_0$  is the linear index, given by  $n_0^2 = 1 + P^{(1)}/\epsilon_0 E$ . The nonlinear index,  $n_2$ , is conventionally defined by

$$n = n_0 + n_2 I_0 \quad (46)$$

where  $I_0$  is the cycle averaged intensity. Choosing the Fourier transform convention such that  $E_0$  is the peak value of the electric field, one has the relationship  $I_0 = n_0 E_0^2 / 2\eta_0$ .

Finally, equating Eqs. (45) and (46), and evaluating at  $\omega_0$ , gives

$$n_2(\omega_0) = \frac{3}{4} \frac{\eta_0}{n_0(\omega_0)^2} \sum_s \frac{q_s^2}{m_s^2} \frac{\omega_{ps}^2}{\mathcal{D}_s^*(\omega_0)\mathcal{D}_s(\omega_0)^3} b_s \quad (47)$$